

Interfacial Chemistry Effects in the Electrochemical Performance of Silicon Electrodes under Lithium-Ion Battery Conditions

Xiangdong Xu, Daniel Martín-Yerga,* Nicholas E. Grant, Geoff West, Sophie L. Pain, Minkyung Kang, Marc Walker, John D. Murphy, and Patrick R. Unwin*

Understanding the solid electrolyte interphase (SEI) formation and (de)lithiation phenomena at silicon (Si) electrodes is key to improving the performance and lifetime of Si-based lithium-ion batteries. However, these processes remain somewhat elusive, and, in particular, the role of Si surface termination merits further consideration. Here, scanning electrochemical cell microscopy (SECCM) is used in a glovebox, followed by secondary ion mass spectrometry (SIMS) at identical locations to study the local electrochemical behavior and associated SEI formation, comparing Si (100) with a native oxide layer (SiO_x/Si) and etched with hydrofluoric acid (HF-Si). HF-Si shows greater spatial electrochemical heterogeneity and inferior lithiation reversibility than SiO_x/Si . This is attributed to a weakly passivating SEI and irreversible lithium trapping at the Si surface. Combinatorial screening of charge/discharge cycling by SECCM with co-located SIMS reveals SEI chemistry as a function of depth. While the SEI thickness is relatively independent of the cycle number, the chemistry – particularly in the intermediate layers – depends on the number of cycles, revealing the SEI to be dynamic during cycling. This work serves as a foundation for the use of correlative SECCM/SIMS as a powerful approach to gain fundamental insights on complex battery processes at the nano- and microscale.

development of portable electronic devices and electric vehicles, and provide opportunities to balance electricity generation and consumption in smart grids.^[1,2] Further applications demand batteries with higher capacity, energy and power densities, and longer operational lifetimes. In this regard, silicon (Si) is a promising negative electrode material due to the higher theoretical specific capacity (3590 mAh g^{-1} , $\text{Li}_{15}\text{Si}_4$) than graphite (372 mAh g^{-1} , LiC_6).^[3–6] However, Si suffers from massive volume expansion ($\approx 400\%$) upon lithiation, leading to cracking and subsequent pulverization, loss of electric contact, and side reactions.^[7] In fact, the formation of the solid-electrolyte interphase (SEI) on Si is highly dynamic^[8] with compositional and structural changes upon cycling due to a so-called “breathing effect”.^[9,10] This particular behavior results in a weakly passivating SEI and systemic loss of Li^+ inventory.^[11] Several strategies have been explored to improve the passivation and stability of the SEI, including the use of additives such as fluoroethylene carbonate,^[12] or the fabrication of artificial SEI layers.^[13,14] Yet, these approaches require additional components or manufacturing steps, further complicating the system.


1. Introduction

Lithium-ion batteries (LiBs) are a key energy storage technology to achieve a low-carbon economy. LiBs have enabled the

fabrication of artificial SEI layers.^[13,14] Yet, these approaches require additional components or manufacturing steps, further complicating the system.

X. Xu, D. Martín-Yerga, P. R. Unwin
Department of Chemistry
University of Warwick
Coventry CV4 7AL, UK
E-mail: daniel.martin-yerga@warwick.ac.uk; p.r.unwin@warwick.ac.uk
D. Martín-Yerga, P. R. Unwin
The Faraday Institution
Quad One
Harwell Campus, Didcot OX11 0RA, UK

N. E. Grant, S. L. Pain, J. D. Murphy
School of Engineering
University of Warwick
Coventry CV4 7AL, UK
G. West
Warwick Manufacturing Group
University of Warwick
Coventry CV4 7AL, UK
M. Kang
School of Chemistry
University of Sydney
Sydney, NSW 2006, Australia
M. Walker
Department of Physics
University of Warwick
Coventry CV4 7AL, UK

 The ORCID identification number(s) for the author(s) of this article can be found under <https://doi.org/10.1002/sml.202303442>

© 2023 The Authors. Small published by Wiley-VCH GmbH. This is an open access article under the terms of the Creative Commons Attribution License, which permits use, distribution and reproduction in any medium, provided the original work is properly cited.

DOI: 10.1002/sml.202303442

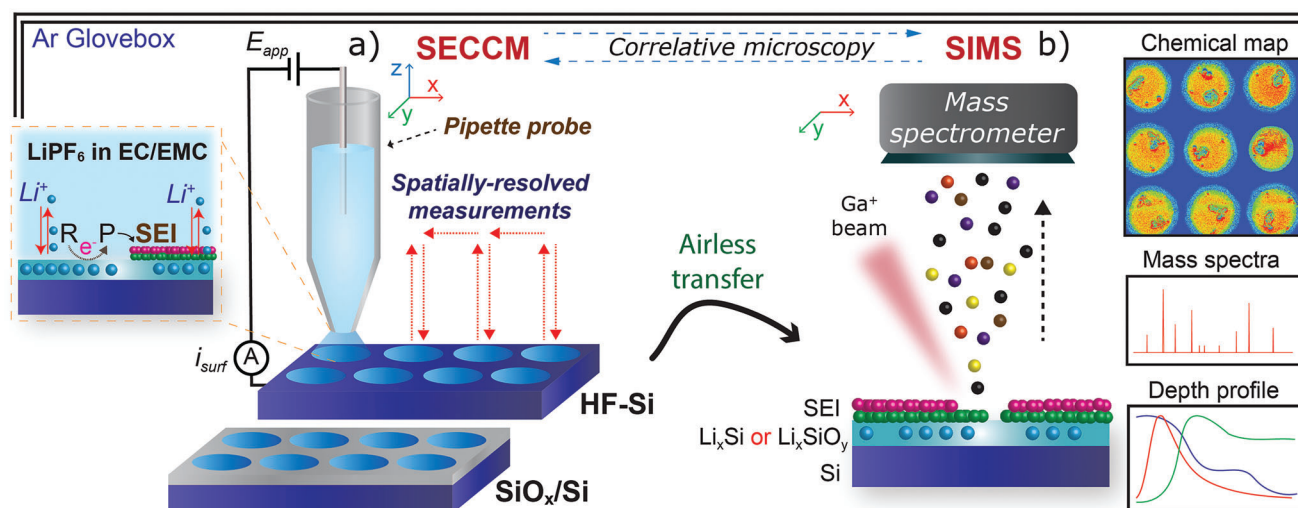


Figure 1. Schematic of correlative electrochemical multi-microscopy approach to study SEI formation and electrochemical processes on SiO_x/Si and HF-Si electrodes: a) hopping-mode SECCM for spatially-resolved electrochemical measurements with a pipette probe filled with 1 M LiPF₆ in EC/EMC, followed by b) SIMS analysis of SEI and Si interfaces in the SECCM regions by the collection of mass spectra and chemical maps as a function of depth into the sample using Ga⁺ sputtering.

Si reacts readily with oxygen forming a surface layer of Si oxides either by contact with air (native oxide) or through synthetic methods.^[15–19] The oxide formation process determines properties such as the state of oxidation, relative oxide composition, and ionic conductivity.^[16,20,21] Chemical etching methods employed to remove the oxide layer, akin to those extensively used in photovoltaic manufacturing,^[22] also vary and thus yield distinct surface properties (e.g., chemical terminations).^[23–27] Recent studies have investigated the effect of the surface oxide layer on Si (e.g., existence,^[15,28] thickness,^[15,17,19,28–30] composition,^[16,29] crystallinity,^[18,29] oxidation method^[16,18]) on the SEI formation and battery performance. Differences in composition, such as the formation of LiSi_xO_y through lithiation of SiO_x, have been shown to provide higher structural stability and longer lifetime.^[28,31] A more stable SEI, resulting in fewer side reactions and higher Coulombic efficiency, has been observed on Si with surface oxides.^[32,33,34] These studies have shown that subtle differences in Si surface properties can strongly influence battery performance and degradation, but important interfacial phenomena require deeper understanding. For instance, it is unclear whether oxide growth and removal processes lead to spatial heterogeneity in properties across the Si surface affecting the electrochemical performance (i.e., the generation of degradation “hot spots”). Local electrochemical measurements are most effective in revealing such phenomena, as illustrated by scanning electrochemical microscopy studies of local discontinuities in the SEI across a Si electrode ascribed to SEI cracking,^[35] and the local initiation of SEI growth on nearly atomically flat Si electrodes.^[36]

Direct correlation between local structure and function (activity) of electrochemical materials with high spatial resolution^[37] can be achieved by combining scanning electrochemical cell microscopy (SECCM) with co-located surface characterization.^[38–41] SECCM has been applied to reveal the heterogeneous (de)lithiation activity on LiFePO₄ composites,^[42,43] individual LiMn₂O₄,^[44,45] and TiO₂^[46] particles, and to study the

SEI formation on highly oriented pyrolytic graphite (HOPG) surfaces.^[47] Recently, we introduced correlative SECCM with shell-isolated nanoparticles for enhanced Raman spectroscopy (SHINERS) to provide information on the SEI chemistry and to reveal the dynamics of SEI formation on Si electrodes,^[8] and with high-resolution cross-sectional imaging to visualize atomic-scale localized degradation.^[48] Novel developments to combine SECCM in tandem with techniques able to provide comprehensive surface chemistry information at commensurate regions are expected to open new avenues to deepen understanding of battery processes such as SEI formation mechanisms at the nano- and micro-scales.

Here, we advocate a correlative electrochemical multi-microscopy approach coupling SECCM and secondary ion mass spectrometry (SIMS), as illustrated in **Figure 1**, to understand the effect of surface chemistry and local interfacial properties on the SEI formation and (de)lithiation performance of native oxide silicon (SiO_x/Si) and hydrofluoric acid etched silicon (HF-Si). A key finding from our study is that the removal of the native oxide layer leads to much worse lithiation reversibility and higher spatial variability in the electrochemical response, SEI properties, and chemistry. Overall, this work reinforces the versatility of SECCM as a leading tool for characterizing battery materials. Combining SECCM with co-located chemical imaging techniques results in a compelling platform for monitoring and analyzing battery interphases.

2. Results and Discussion

2.1. Comparison of Local Electrochemistry on SiO_x/Si and HF-Si

Structural heterogeneities and surface oxide termination can affect the SEI formation and (de)lithiation behavior of Si battery materials.^[6,21] We thus analyzed these processes, comparing the behavior of SiO_x/Si and HF-Si electrodes. SECCM was used to

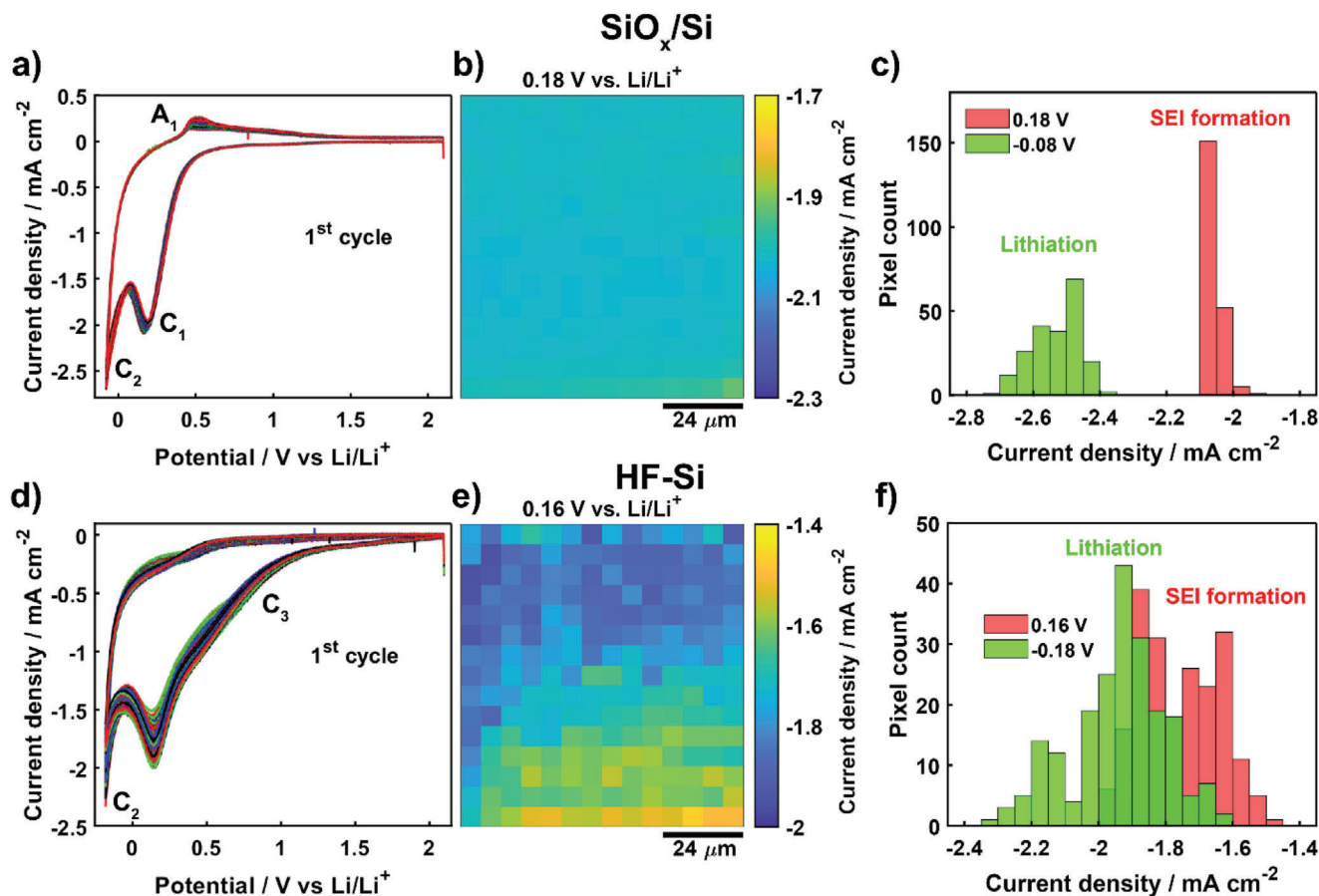


Figure 2. Summary of main results obtained from voltammetric SECCM imaging of a–c) SiO_x/Si and d–f) HF-Si electrodes using pipettes with diameters of 2.1 μm (SiO_x/Si) and 2.7 μm (HF-Si) filled with 1 M LiPF₆ in EC/EMC. Voltammetric data obtained for the first charge/discharge cycle in all the SECCM pixels of a) SiO_x/Si and d) HF-Si. Potential ranges were between +2.10 and –0.08 V versus Li/Li⁺ for SiO_x/Si and between +2.10 and –0.18 V versus Li/Li⁺ for HF-Si. Equipotential maps representing spatially-resolved current densities of electrolyte reduction (C₁ process) on b) SiO_x/Si at +0.18 V and on e) HF-Si at +0.16 V. Scale bars are 24 μm. Histogram for current densities of electrolyte reduction (C₁) and lithiation (C₂) obtained from SECCM maps for c) SiO_x/Si and f) HF-Si.

record two voltammetric charge/discharge cycles at 210 independent locations (pixels) across the two surfaces (covering areas of 84 × 90 μm in each case). All the spatially-resolved voltammetric responses (first cycle) recorded on SiO_x/Si by SECCM are shown in Figure 2a, where the faradaic processes are assigned to electrolyte reduction (C₁, origin of SEI formation), lithiation (C₂), and delithiation (A₁).^[19,20,34,49,50] Partial reduction of the native oxide layer has been previously reported,^[33,34] but no signs of this process were detected on the cyclic voltammetry (CV) profile. The current density map at +0.18 V versus Li/Li⁺ (Figure 2b) shows a relatively uniform response for electrolyte reduction on SiO_x/Si, further demonstrated by plotting the distribution of current densities (Figure 2c). Lithiation (–0.08 V) and delithiation (+0.47 V, forward sweep) activity maps are shown in Figure S1a,b, Supporting Information. SECCM left uniform-sized footprints (≈3.8 μm diameter) on SiO_x/Si as shown by SEM (Figure S1c, Supporting Information), which proves that meniscus contact was stable during experiments.

CV profiles from SECCM imaging of HF-Si (Figure 2d, first cycle) showed a new cathodic process (C₃) at around +0.9 V, a detectable shift in potential for the electrolyte reduction peak

(C₁) (+0.16 V on HF-Si vs +0.18 V on SiO_x/Si), and the absence of any delithiation process (A₁). We attribute C₃ to the formation of Si-ethoxy surface intermediates due to electrolyte decomposition.^[51] Linear carbonates can decompose to ethoxy radicals (RO·) or anions (RO[–]) leading to the substitution of protons on hydrogen-terminated Si (Si-H) by ethoxy groups,^[51,52] a process that is blocked by the oxide layer on SiO_x/Si.^[51] A more negative overpotential is required to achieve lithiation current densities on HF-Si of the same magnitude as on SiO_x/Si, due to the existence of surface hydrogen termination.^[32,53] HF-Si displayed a more heterogeneous response as shown in the current density map for C₁ at +0.16 V (Figure 2e) and the corresponding histogram (Figure 2f), with again a very consistent SECCM footprint (≈5.0 μm diameter, Figure S2a, Supporting Information). Indeed, the average current density for HF-Si (C₁ process) was -1.76 ± 0.12 mA cm⁻², the standard deviation is approximately six times larger than for SiO_x/Si: -2.05 ± 0.02 mA cm⁻². A lithiation activity map (current density at C₂, –0.18 V) is also shown in Figure S2b, Supporting Information. Variability in the electrochemical response for HF-Si is even more pronounced on the second charge/discharge cycle (Figure S3, Supporting

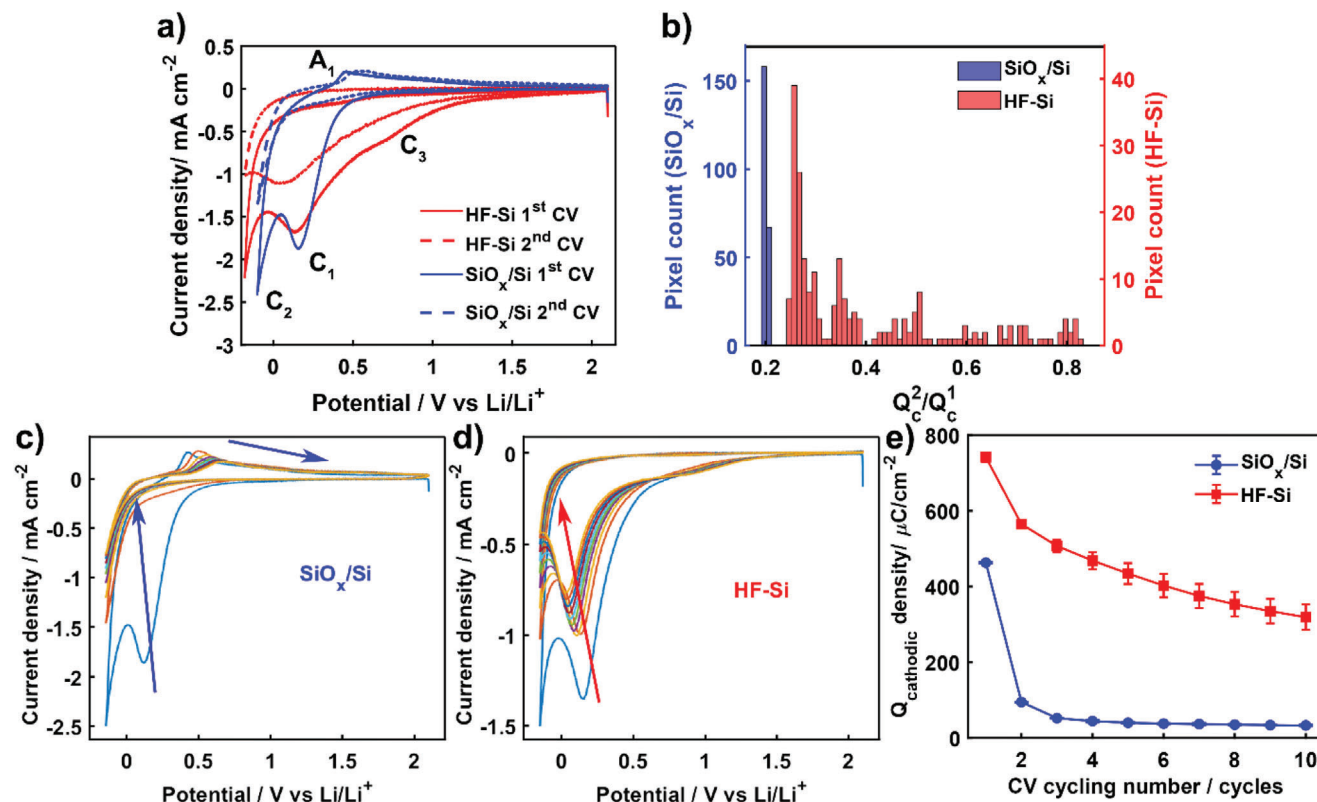


Figure 3. a) Representative voltammetric profiles for the first (solid line) and second (dashed line) charge/discharge cycles on HF-Si (red line) and SiO_x/Si (blue line) extracted from individual SECCM locations. b) Histogram of the ratio between cathodic charge (Q_c) from the second and first charge/discharge cycles (Q_c^2/Q_c^1) obtained from all SECCM locations ($n = 210$) on SiO_x/Si and HF-Si. Representative voltammetric profiles for 10 charge/discharge cycles recorded at one individual location on c) SiO_x/Si and d) HF-Si. Arrows indicate the direction of increasing cycle number. e) Evolution of average cathodic charge (Q_c) as a function of charge/discharge cycle number calculated from all the SECCM locations ($n = 36$) on SiO_x/Si and HF-Si.

Information). The increased heterogeneity on HF-Si is tentatively ascribed to local variations in surface properties, such as hydrogen termination or minor structural defects generated during the removal of the surface native oxide layer.^[54,55] Changes in surface roughness or wettability should not be major contributors to the different responses observed between SiO_x/Si and HF-Si. The surface remains relatively flat following the etching process,^[24] and both SiO_x/Si and HF-Si exhibit similar surface wettability (evidenced by the ratio of SECCM footprint to pipette diameter, $d_{\text{footprint}}/d_{\text{pipette}}$, of 1.8 and 1.9, respectively). While such local variations in activity at the nano/microscale would tend to be undetected by conventional experiments, spatially-resolved SECCM is able to reveal this important information.

2.2. SEI at Early Stages is Strongly More Passivating on SiO_x/Si than on HF-Si

To further highlight the distinct electrochemical response of SiO_x/Si and HF-Si, representative CVs for the first and second cycles are shown in Figure 3a. The main differences between the responses of the two surfaces for the first cycle were described above, and now we focus on the behavior for the second

charge/discharge cycle, after the initial formation of the SEI. The electrolyte reduction process (C_1) largely disappeared in the second cycle on SiO_x/Si whereas all processes were preserved on HF-Si but with a small decrease in current density. Thus, the SEI formed at the very early stages (first cycle) is more passivating on SiO_x/Si , as further electrolyte reduction is blocked more efficiently.

A semi-quantitative analysis of the passivating efficiency of the early SEI layer was carried out by integrating the cathodic charge (Q_c) from all the pixels in SECCM scans. Figure 3b shows the population distribution for the ratio between Q_c from the second and first cycles (Q_c^2/Q_c^1), which provides relative information about how much electrolyte reduction is prevented on the second charge/discharge cycle by the SEI formed during the first cycle. Homogeneous values of $Q_c^2/Q_c^1 \approx 0.2$ were found across the SiO_x/Si surface whereas the distribution was wider (0.25 to 0.85) for HF-Si, which again reveals the spatial variability of HF-Si, in this case with respect to the passivating properties of the SEI. These results demonstrate there are some regions on HF-Si where the SEI is either particularly unstable or does not prevent electrolyte reduction efficiently. Notably, for all surface locations, Q_c^2/Q_c^1 was higher on HF-Si than on SiO_x/Si . Evidently, the native oxide layer in SiO_x/Si aids in developing a more passivating SEI in the very early stages.

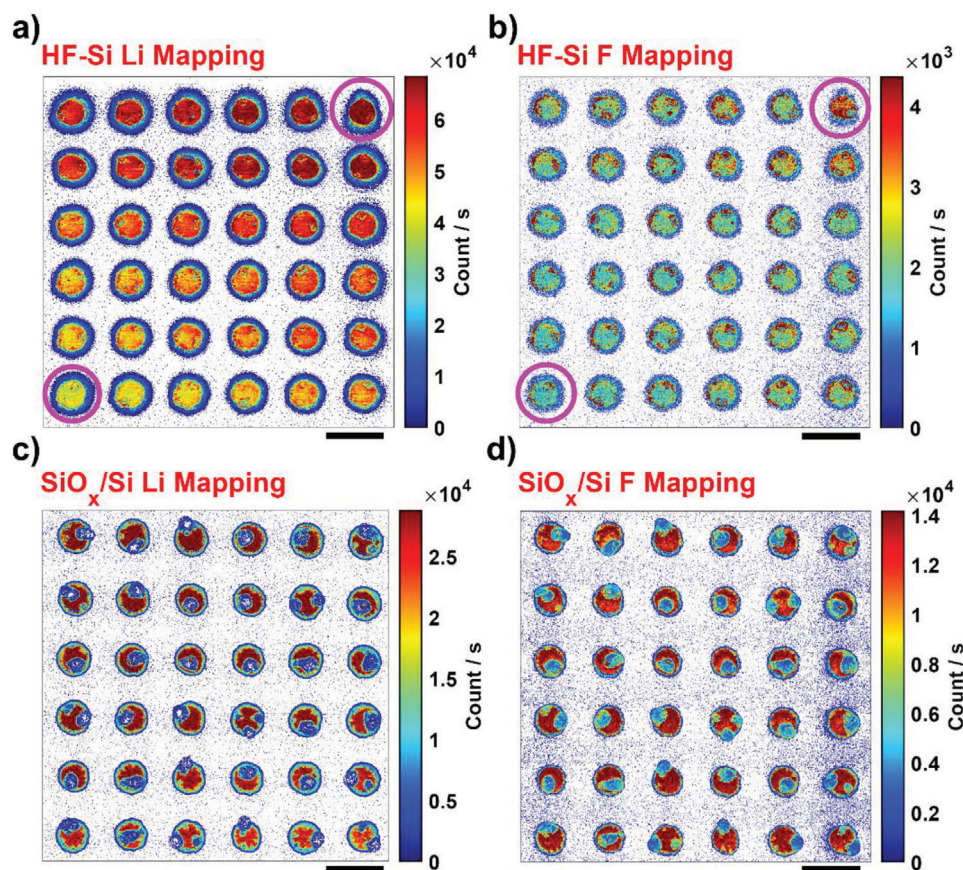


Figure 4. a,c) Li^+ and b,d) F^- maps obtained by SIMS from a,b) HF-Si and c,d) SiO_x/Si electrodes after SECCM with 10 charge/discharge voltammetric cycles. SIMS maps were collected using a 30 keV Ga^+ ion beam with a primary ion beam current of 10 pA at a resolution of 55 nm. Scale bars are 7 μm . Detailed SECCM results and conditions are presented in Figures S5 and S6, Supporting Information. Crystals after electrolyte drying are detected as spots with lower Li^+ and F^- concentrations on SiO_x/Si maps but were not considered for analysis.

The evolution of SEI formation was then monitored by recording SECCM experiments up to 10 charge/discharge cycles on SiO_x/Si and HF-Si (main SECCM results summarized in Figures S4 and S5, Supporting Information). Figure 3c shows the multi-cycling voltammetric response at one location on SiO_x/Si and the response on HF-Si is shown in Figure 3d. Voltammetric processes related to electrolyte reduction (C_1) disappeared completely after the third cycle for SiO_x/Si together with an initial decrease in lithiation (C_2) current density that became nearly stable by the fifth cycle.

The delithiation peak (A_1) shifted to more positive potentials upon cycling (Figure S4b, Supporting Information), showing more sluggish charge transfer kinetics due to a lower conductivity as a consequence of the formation of amorphous Si and the SEI layer.^[34] In contrast, significant current density was still obtained for C_1 on HF-Si even at the tenth cycle. C_3 was not strongly affected by cycling (Figure 3d), whereas the current density for C_1 (electrolyte reduction) and C_2 (lithiation) slowly decreased upon cycling the HF-Si electrode. No delithiation processes were observed for HF-Si even after several cycling steps, confirming the poor lithiation reversibility of HF-Si.

The evolution of Q_c upon cycling (Figure 3e) provides clear evidence of the different behavior for electrolyte reduction and, in-

directly, of the passivating properties of the SEI on SiO_x/Si compared to that on HF-Si. A sharp decrease in Q_c during the first three cycles indicates that the SEI formed on SiO_x/Si is more passivating and is efficient in preventing further electrolyte reduction, in contrast to the more gradual decrease observed on HF-Si, due to either slow SEI formation or an SEI formed by components with weak passivating properties.

2.3. Correlative SIMS Imaging Uncovers Local SEI Chemical Heterogeneities on HF-Si

To elucidate differences in the spatial heterogeneities observed between HF-Si and SiO_x/Si , correlative chemical analysis by SIMS was carried out to collect Li^+ (Figure 4a–c) and F^- (Figure 4b–d) maps from the top of the SEI layer on commensurate areas to SECCM after 10 charge/discharge cycles. Spatial differences in SEI chemistry from the HF-Si and SiO_x/Si SIMS maps are evident. For instance, Li^+ and F^- signals increased from the bottom-left to the top-right regions of the HF-Si surface. Correlating this behavior with the CVs (first charge/discharge cycle) of the first (bottom left) and last (top right) SECCM spots (marked with magenta circles in Figure 4a,b), the main

difference comes in the current density of the C_3 process appearing at approximately +0.73 V as shown in Figure S5a,b, Supporting Information. This process is potentially assigned to the formation of Si-ethoxy surface intermediates by electrolyte decomposition and reaction with hydrogen-terminated Si (Si-H).^[51] These local heterogeneities across the HF-Si surface are thus likely due to the existence of different degrees of hydrogen termination resulting from the etching process.^[26,27,56–58] Our SIMS results indicate that these heterogeneities not only lead to some variation in electrochemistry, as shown in Figure S5, Supporting Information but also to different SEI chemistry, with higher reactivity (i.e., current density for C_3) promoting the enrichment of Li^+ and F^- on the top layer of the SEI. In contrast, relatively homogeneous Li^+ (Figure 4c) and F^- (Figure 4d) SIMS maps are found on SiO_x/Si , consistent with the strongly uniform SECCM response across the SiO_x/Si surface (Figure S5, Supporting Information); the absence of Si-H terminations means that the reaction mentioned above does not occur. Note that the sample was not washed with any organic solvents to keep the pristine structure and composition of the SEI layer and the electrolyte residues observed on SiO_x/Si footprints (shown as lower Li^+ and F^- concentrations than the SEI) were not considered for the analysis.

2.4. Chemistry of SEI Intermediate Layers is Highly Dynamic during SEI Formation

The SEI comprises a layered structure with the top layers composed mainly of organic species and the bottom layers being richer in inorganic species,^[33,59,60] although an inverted structure has been reported on etched Si surfaces.^[61] The SEI on Si may also show a dynamic “breathing” characteristic with the composition changing upon cycling.^[8,25,33,62] To understand the effect of cycling on the SEI chemistry, we carried out combinatorial SECCM with each row corresponding to a different number of charge/discharge cycles (from 1 to 10) and Li^+ SIMS mapping was undertaken with a sequence of sputtering steps (i.e., depth profiling), up to the complete removal of the SECCM footprint (Figure S6, Supporting Information). This produced SIMS maps from the top SEI layer down to the Si interface. All the SECCM footprints remaining after each step of the sputtering sequence (Figure S6, Supporting Information) appear to be similar and thus the SEI thickness is considered to be fairly independent of the number of charge/discharge cycles, within the range studied (1–10 cycles). In addition, the analysis of cross-sections (Figure S7, Supporting Information) taken from representative SECCM spots after 10 cycles revealed a thicker SEI on HF-Si (≈ 100 nm) compared to SiO_x/Si (≈ 50 nm), although this thickness value can vary slightly depending on the location due to the inherent roughness of the SEI. This difference implies that each corresponding SIMS map from the sputtering sequence likely provides information into distinct layers within the stratified structure of the SEI. As such, a direct comparison between Si samples was not carried out in this study.

Selected layers of Li^+ SIMS maps for HF-Si are shown in Figure 5a–d, with the full sequence in Figure S8, Supporting Information. The top Li^+ SIMS layer (Figure 5a), believed to be dominated by organic components,^[33,59] was similar for all the charge/discharge cycle numbers. However, from the second

SIMS layer on, towards the electrode, the relative Li^+ concentration was dependent on the number of charge/discharge cycles. For instance, the second, third, and tenth cycles showed the highest Li^+ concentration at the second Li^+ SIMS layer (Figure S8, Supporting Information), whereas the fifth, sixth, and eighth cycles showed the highest Li^+ concentration in the fourth SIMS layer (Figure 5b). Towards the Si interface, Li^+ concentration became more or less independent of the number of charge/discharge cycles.

Similar behavior with cycle number-dependent Li^+ concentration at intermediate SIMS layers analyzed in the SEI was also observed for SiO_x/Si (Figure 5e–h, and full sequence in Figure S9, Supporting Information). SEI formation on Si electrodes, irrespective of the initial surface chemistry, results in a composition that is more heterogeneous in Li-based species for intermediate layers analyzed by SIMS, as summarized in Figure S10, Supporting Information. Note that regions where electrolyte crystals are deposited (identified as a lower Li^+ signal in SIMS but higher C, F, and P signals in EDS as shown in Figure S11, Supporting Information) were not considered for this analysis.

SIMS spectra were recorded for 10-cycle SECCM experiments on both SiO_x/Si and HF-Si to identify the main chemical compounds over a range of $m/z = 0.4$ –100 for both positive (Figure S12a,b, Supporting Information) and negative (Figure S12c,d, Supporting Information) polarity. Several chemical fragments were tentatively assigned to surface functional groups and SEI components, as outlined in Table S1, Supporting Information for positive ions and Table S2, Supporting Information for negative ions. Evolution of the normalized signals, as a function of depth profile number, for negative ($m/z = 25, 45, 63, 76$) and positive ($m/z = 28$) fragments, corresponding to SEI components (C_2H^- , LiF_2^- , PO_2^-) and Si surface (SiO_3^- , Si^+) is highlighted in Figure S13, Supporting Information. Relative signals from SEI components show significant fluctuations, which is ascribed to the complex and heterogeneous composition of the SEI layer on Si electrodes.^[8] Although the aforementioned fragments for the SEI and surface components were observed on both HF-Si and SiO_x/Si , the signal evolution as a function of depth was different for each electrode, consistent with the different SEI thickness and the distinct evolution of the electrochemistry on each surface.^[25,33,34]

2.5. Significant Li Trapping on HF-Si Explains the Poor Lithiation Reversibility

We now explore the physicochemical basis of the difference in lithiation reversibility between SiO_x/Si and HF-Si electrodes. Figure 6 shows Li^+ SIMS maps of two representative SECCM spots for HF-Si (marked with a magenta circle in Figure 5a) and SiO_x/Si (marked with a black circle in Figure 5e) corresponding to 10 charge/discharge cycles and the deepest sputtered layer (full sputtering sequence in Figures S14 and S15, Supporting Information). These sputtering conditions completely removed the SECCM footprint as shown in Figure S6, Supporting Information, enabling the analysis of the Si interface. Indeed, cross-sectional imaging confirms that the analyzed regions in both samples correspond to the Si material below the SEI/Si interface (as depicted in Figure S16, Supporting Information). These

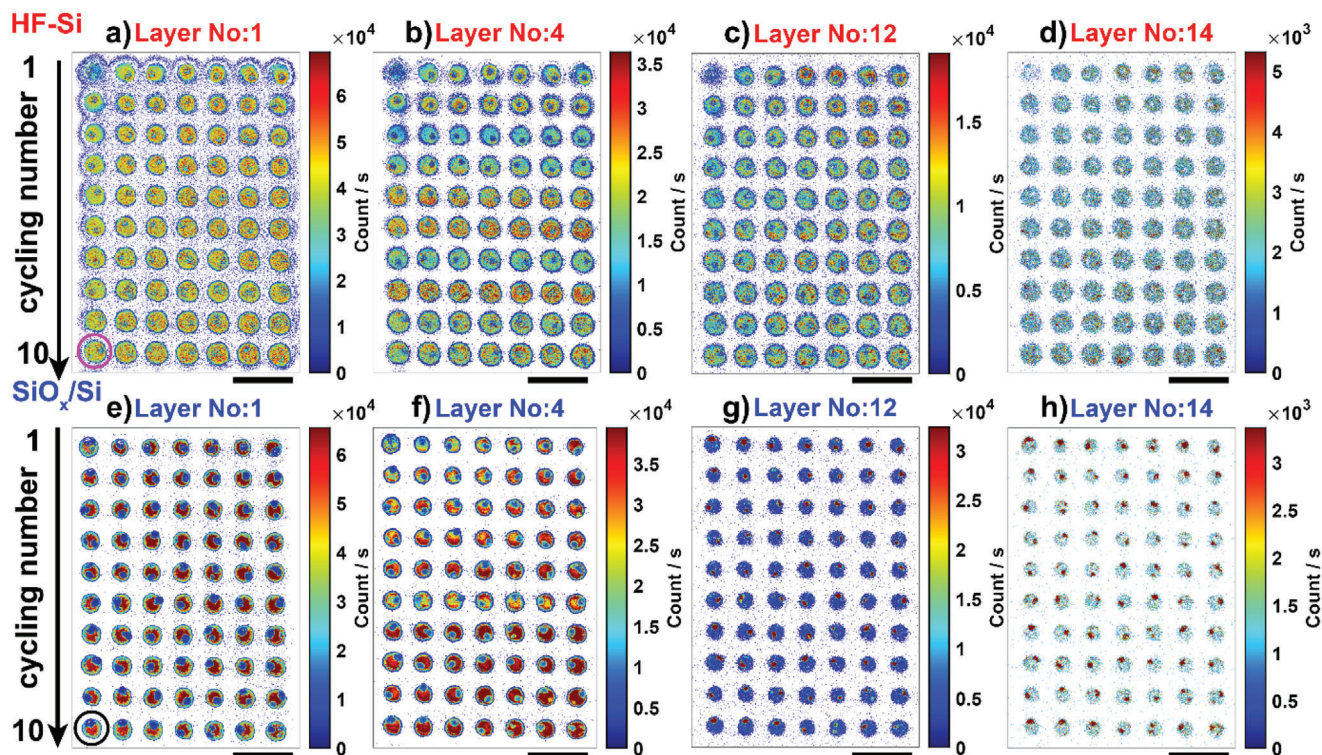


Figure 5. Li^+ maps obtained by SIMS as a function of sputtering step (i.e., depth) after combinatorial SECCM experiments of the increasing number of voltammetric charge/discharge cycles for a-d) HF-Si and e-h) SiO_x/Si . Selected sputtering steps were the first, fourth, twelfth, and fourteenth, with the full sequence shown in Figures S8 and S9, Supporting Information. The number of SECCM voltammetric charge/discharge cycles changes sequentially from 1 (top row) to 10 (bottom row). Scale bars are 14 μm .

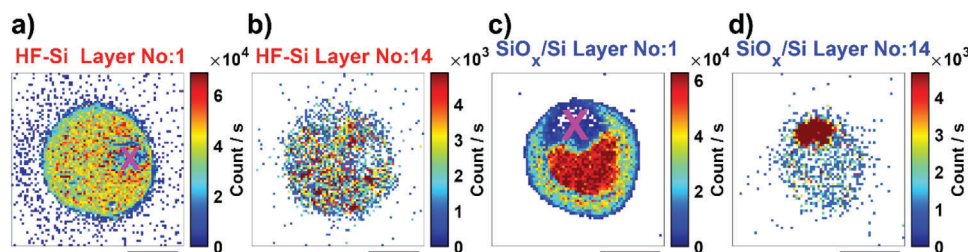


Figure 6. Li^+ maps obtained by SIMS for the first and fourteenth sputtering step on a specific location of a,b) HF-Si and c,d) SiO_x/Si after SECCM for 10 charge/discharge cycles. Crosses in magenta color indicate areas with electrolyte crystals that were not considered for analysis. Scale bars are 2 μm .

regions lie $\approx 42\text{--}45$ nm beneath the Si surface prior to any sputtering. As such, Li^+ SIMS signals originate from Li trapped within the Si material following the delithiation step. Note that regions, where electrolyte crystals were deposited, were not considered for these analyses. Li^+ concentration at the Si interface (fourteenth sputtering layer) was clearly higher on HF-Si than on SiO_x/Si , indicating significant Li trapping on HF-Si that is consistent with the absence of voltammetric delithiation peaks.^[63] Lithiation on HF-Si directly involves the formation of amorphous Li_xSi species^[64] whereas the initial reaction on SiO_x/Si results in the formation of Li_xSiO_y by Li^+ reaction with the native oxide layer, and subsequent formation of Li_xSi after Li passes through the oxide layer.^[33,49] Our SECCM conditions, that is, relatively fast scan

rates, will probe interfacial and fast (de)lithiation processes and are thus sensitive to the detection of differences between HF-Si and SiO_x/Si . The Li^+ diffusivity rate in Li_xSi has been reported to be two orders of magnitude higher than in Li_xSiO_y .^[65] Voltammetric analysis in tandem with SIMS clearly indicates Li trapping on HF-Si, which might come from fast Li^+ diffusion into bulk Si that will be unavailable for delithiation. In contrast, Li accumulates as Li_xSiO_y on the surface of SiO_x/Si , leading to more Li^+ available near the interface for delithiation. $\text{Li}_2\text{Si}_2\text{O}_5$ has been reported as the most favorable Li silicate formed on SiO_2 based on calculations of free energies of reaction.^[66,67] The native oxide layer in SiO_x/Si is formed by around 90% SiO_2 (as a ratio of $\text{SiO}_2:\text{SiO}_x$, see Figure S17 and Tables S3 and S4, Supporting

Information for X-ray photoelectron spectroscopy analysis). Lithiation of SiO_2 to $\text{Li}_2\text{Si}_2\text{O}_5$ is reversible, thereby contributing to delithiation processes observed on SiO_x/Si .^[68]

3. Conclusion

In conclusion, we have rationalized the distinct local electrochemical response on SiO_x/Si and HF-Si at the microscale by a novel correlative multi-microscopy approach based on SECCM with co-located SIMS. This approach enabled the study of key phenomena such as spatial heterogeneity of the electrochemical response, local SEI formation, chemistry, and dynamics (as inferred from depth profiling), and Li^+ trapping on Si surfaces with high resolution. SiO_x/Si exhibited a more uniform electrochemical response across the surface, a strongly passivating SEI, and lower Li trapping, leading to superior lithiation reversibility than HF-Si. While the SEI thickness was more or less independent of the number of voltammetric cycles in the early formation stages, the composition was strongly dependent on cycle number, notably in the intermediate layers of the SEI analyzed by SIMS, indicating an evolution of the composition with time.

Our main finding exposes the beneficial role of the native oxide layer on the electrochemical performance of Si electrodes for LIBs. Correlative SECCM/SIMS microscopy is demonstrated as a powerful approach to understanding complex battery processes combinatorially and at a local scale. This approach presents huge opportunities to reveal fresh insights into structure-function relationships in battery materials. In addition, our study of model Si materials lays the groundwork for future investigations that aim to elucidate the intricate interplay of surface effects from individual components (e.g., active material, binder, conductive carbon) by spatially-resolved characterization of more conventional battery electrodes. Ultimately, these new insights could inform the rational design of highly efficient battery interfaces.

4. Experimental Section

Materials and Chemicals: SiO_x/Si electrodes consisted of a ~ 1 nm thick native oxide layer on the surfaces of pieces of a mechanically polished 520 μm thick (100)-oriented float-zone 7 Ωcm n -type silicon wafer. The thickness of the native oxide layer was estimated from a recent study by Grant et al.^[69] To investigate the SEI formation on bare silicon surfaces, the native oxide layer on sister silicon samples was removed by etching in a solution mixture of 2 vol.% HF (50 wt.%) and 2 vol.% hydrochloric acid (37 wt.%) for 5 min, herein denoted HF-Si. Details of the preparation and characterization of HF-Si could be found elsewhere,^[24] including topography measurements that revealed a relatively flat surface even after a slightly extended treatment duration. HF-Si samples were stored in an Ar-filled glovebox (< 0.1 ppm H_2O and O_2 levels) immediately after etching and SECCM experiments were carried out on the same day (typically completed within 5 h of sample preparation) to minimize organic contamination and surface oxidation. An electrical connection was established by placing copper tape on the bottom side of the Si wafer.

Battery-grade electrolyte consisting of 1 M LiPF_6 dissolved in a mixture of ethylene carbonate and ethyl methyl carbonate (EC:EMC, 1:1 vol. ratio) was purchased from Sigma-Aldrich. Silver wire (99.99+%, 0.25 mm diameter) was purchased from Goodfellow.

Scanning Electrochemical Cell Microscopy (SECCM): SECCM measurements were performed on a home-built instrument described in detail

elsewhere.^[37,39,40] The SECCM instrument, placed on an anti-vibration table, was set up in an Ar-filled glovebox (MBraun MB200B/MB20G), where O_2 and H_2O levels were less than 0.1 ppm. The SECCM setup was enclosed with a copper mesh (Faraday cage) to minimize noise from electromagnetic interference, and the glovebox vacuum pump and circulation system were turned off to minimize mechanical vibration. Data acquisition and instrument control were achieved via an FPGA card (PCIe-7852R, National Instruments) running the Warwick Electrochemical Scanning Probe Microscopy (WEC-SPM, www.warwick.ac.uk/electrochemistry) Platform through a Labview 2019 interface.

Single-barrel pipettes with an opening diameter of ca. 2 μm were made by pulling borosilicate capillaries (GC120F-10, Harvard Apparatus; with 1.2 and 0.69 mm outer and inner diameters) with a laser-based pipette puller (P-2000, Sutter Instruments). Pipettes were filled with 1 M LiPF_6 in EC:EMC and an Ag wire was inserted from the back, at least 3–4 cm from the tip end,^[70] to serve as a quasi-reference counter electrode (QRCE), and then mounted on an x,y,z-piezoelectric positioner (P-611.3S Nanocube, Physik Instrumente) for fine movement. The pipette was placed near the Si sample, which acted as a working electrode, with a coarse micro-positioner (M-461-XYZ-M, Newport). The SECCM schematic in Figure 1a illustrates the automated hopping mode used as the scanning protocol for spatially-resolved cyclic voltammetry (CV) measurements. Briefly, the pipette was moved by the piezoelectric positioner to approach the surface with a bias potential ($-E_{\text{app}}$) applied between the QRCE and the Si electrode of, typically, +2.10 V versus Li/Li^+ (Ag QRCE potential was converted to the Li/Li^+ scale after calibration with the ferrocene redox process).^[47] Surface (working electrode) current (i_{surf}) was monitored and used as a feedback signal to stop the vertical motion of the pipette once the contact between the liquid meniscus from the pipette tip and the Si surface was detected (when i_{surf} was above 2.75 pA). The pipette itself did not contact the surface. For a typical experiment, the potential was swept between +2.10 and -0.08 V versus Li/Li^+ for SiO_x/Si and between +2.10 and -0.18 V versus Li/Li^+ for HF-Si at a scan rate of 1 V s^{-1} , to record a cyclic voltammogram. When an individual measurement ended, the pipette was retracted and moved to the next location on the Si surface with a separation of 6 μm (to avoid overlap of adjacent spots), and a new measurement was recorded. The same procedure was repeated at a series of predefined locations (i.e., individual pixels) across the Si electrodes. For rare false approach spots, where the pipette meniscus did not contact the surface, data in those locations were estimated as the average of data from neighboring SECCM spots in the current density maps (in filling), but these points were excluded from distribution analyses (i.e., histograms). These events were rare, for example, only one spot for SiO_x/Si maps (Figure S1c, Supporting Information), and two spots for HF-Si maps (Figure S2a, Supporting Information).

Physicochemical Characterization: SECCM footprints were characterized by a dual-focused ion beam and scanning electron microscopy system (FIB-SEM, FEI Scios). Fiji/ImageJ was used via the function “Analyze Particles” to automatically detect and measure the contact area from all individual SECCM measurement spots (Figure S18, Supporting Information) and used for the evaluation of current densities. Energy dispersive X-ray spectroscopy (EDS, X-Max^N 150, Oxford Instruments) was used for elemental mapping of SECCM scanned areas.

Quadrupole secondary ion mass spectroscopy (SIMS, EQS HIDEN Analytical) characterization was performed under high vacuum at a pressure below 5×10^{-6} mbar. SIMS was used for chemical imaging, depth profiling, and mass spectra collection at locations where SECCM measurements were made, as illustrated in Figure 1b. A 30 keV Ga^+ ion beam with a primary ion beam current of 10 pA (six sputtering cycles, 10 ms dwell time), 30 pA (two sputtering cycles, 8 ms dwell time), 50 pA (three sputtering cycles, 5 ms dwell time), and 300 pA (three sputtering cycles, 1 ms dwell time) was applied for depth profiling while imaging Li^+ and F^- ions with a high lateral resolution of 92 nm. An approximate calculation of the depth resolution for this experiment, assuming a homogeneous sputtering rate across the different layers, yielded values of 5.3, 12.7, 13.3, and 15.9 nm (HF-Si) and 3.4, 8.1, 8.4, and 10.1 nm (SiO_x/Si) for each cycle of the 10, 30, 50, and 300 pA experiments, respectively. A 30 keV Ga^+ ion beam with a primary ion beam current of 10 pA (100 ns dwell time) was used for depth profiling while collecting the spectra with a high spectral

resolution of 0.01 amu to analyze the chemical composition as a function of depth. Consequently, the data obtained from both SIMS modalities – mapping and mass spectra collection – could be directly compared as they referred to different surface depths. Samples prepared after SECCM were always transferred from the glovebox to the microscope chamber through an airless transfer kit to prevent side reactions of reactive SEI and electrolyte components.

To determine the SEI thickness and the cross-sectional depth between the pristine Si interface (without sputtering) and the sputtered surface after SIMS for HF-Si and SiO_x/Si samples, a dual beam (FIB-SEM, FEI Scios) was used to prepare the lamella with surface protected by initial electron-beam followed by ion-beam deposition of Pt layers. Then high angle annular dark field (HAADF), and bright field (BF) scanning transmission electron microscopy (STEM, FEI Talos F200X) imaging and EDS analysis (Super-X EDS system) were performed under 200 kV to easily differentiate the Si and SEI interfaces and measure the thickness.

X-ray photoelectron spectroscopy (XPS, Kratos Axis Ultra DLD spectrometer), which was performed with Al K α radiation at a take-off angle of 15° and 90° to the sample surface under high-vacuum ($\approx 10^{-10}$ mbar) conditions, was used to elucidate the chemical composition and bonding configuration.

Supporting Information

Supporting Information is available from the Wiley Online Library or from the author.

Acknowledgements

The authors acknowledge financial support from the EPSRC UK Faraday Institution (EP/S003053/1) through the Characterisation project (FIRG013), and from the European Union's Horizon 2020 research and innovation programme under the Marie Skłodowska-Curie grant agreements no. 812398 (SENTINEL) and no. 101026563 (NANODENDRITE). P.R.U. thanks the Royal Society for a Wolfson Research Merit Award. Work by N.E.G., S.L.P., and J.D.M. was supported by the EPSRC Charge Oxide Inversion Layer (COIL) solar cells project (EP/V037749/1) and the Royal Society (RGS\R2\212150). S.L.P. was supported by an EPSRC Doctoral Training Partnership studentship (EP/R513374/1). M.W. acknowledges financial support from the EPSRC-funded Warwick Analytical Science Centre (EP/V007688/1).

Conflict of Interest

The authors declare no conflict of interest.

Data Availability Statement

The data that support the findings of this study are openly available in Zenodo at <https://doi.org/10.5281/zenodo.7950760>.

Keywords

correlative microscopy, li-ion batteries, scanning probe microscopy, silicon, solid electrolyte interphase

Received: May 19, 2023
Published online: June 3, 2023

- [2] C. P. Grey, D. S. Hall, *Nat. Commun.* **2020**, *11*, 6279.
- [3] F. Zhang, W. Luo, J. Yang, *Chem Asian J* **2020**, *15*, 1394.
- [4] J. Guo, W. Zhai, Q. Sun, Q. Ai, J. Li, J. Cheng, L. Dai, L. Ci, *Electrochim. Acta* **2020**, *342*, 136068.
- [5] Y. Chen, L. Liu, J. Xiong, T. Yang, Y. Qin, C. Yan, *Adv. Funct. Mater.* **2015**, *25*, 6701.
- [6] M. Ashuri, Q. He, L. L. Shaw, *Nanoscale* **2016**, *8*, 74.
- [7] K. Feng, M. Li, W. Liu, A. G. Kashkooli, X. Xiao, M. Cai, Z. Chen, *Small* **2018**, *14*, 1702737.
- [8] D. Martin-Yerga, D. C. Milan, X. Xu, J. Fernandez-Vidal, L. Whalley, A. J. Cowan, L. J. Hardwick, P. R. Unwin, *Angew. Chem., Int. Ed.* **2022**, *61*, 202207184.
- [9] J. D. McBrayer, M.-T. F. Rodrigues, M. C. Schulze, D. P. Abraham, C. A. Appleby, I. Bloom, G. M. Carroll, A. M. Colclasure, C. Fang, K. L. Harrison, *Nat. Energy* **2021**, *6*, 866.
- [10] I. Hasa, A. M. Haregewoin, L. Zhang, W. Y. Tsai, J. Guo, G. M. Veith, P. N. Ross, R. Kostecki, *ACS Appl. Mater. Interfaces* **2020**, *12*, 40879.
- [11] Y. Yin, E. Arca, L. Wang, G. Yang, M. Schnabel, L. Cao, C. Xiao, H. Zhou, P. Liu, J. Nanda, G. Teeter, B. Eichhorn, K. Xu, A. Burrell, C. Ban, *ACS Appl. Mater. Interfaces* **2020**, *12*, 26593.
- [12] Z. Xu, J. Yang, H. Li, Y. Nuli, J. Wang, *J. Mater. Chem. A* **2019**, *7*, 9432.
- [13] R. G. Fedorov, S. Maletti, C. Heubner, A. Michaelis, Y. Ein-Eli, *Adv. Energy Mater.* **2021**, *11*, 2101173.
- [14] Q. Ai, D. Li, J. Guo, G. Hou, Q. Sun, X. Xu, W. Zhai, L. Zhang, J. Feng, P. Si, J. Lou, L. Ci, *Adv. Mater. Interfaces* **2019**, *6*, 1901187.
- [15] G. Zheng, Y. Xiang, L. Xu, H. Luo, B. Wang, Y. Liu, X. Han, W. Zhao, S. Chen, H. Chen, Q. Zhang, T. Zhu, Y. Yang, *Adv. Energy Mater.* **2018**, *8*, 1801718.
- [16] P. R. Abel, Y.-M. Lin, H. Celio, A. Heller, C. B. Mullins, *ACS Nano* **2012**, *6*, 2506.
- [17] B.-C. Yu, Y. Hwa, C.-M. Park, J.-H. Kim, H.-J. Sohn, *RSC Adv.* **2013**, *3*, 9408.
- [18] K. Kong, G. Xu, Y. Lan, C. Jin, Z. Yue, X. Li, F. Sun, H. Huang, J. Yuan, L. Zhou, *Appl. Surf. Sci.* **2020**, *515*, 146026.
- [19] M. Schnabel, S. P. Harvey, E. Arca, C. Stetson, G. Teeter, C. Ban, P. Stradins, *ACS Appl. Mater. Interfaces* **2020**, *12*, 27017.
- [20] M. K. Jangid, S. Sinha, A. S. Lakshmi, F. J. Sonia, A. Kumar, R. O. Dusan, A. Mukhopadhyay, *Electrochim. Acta* **2019**, *297*, 381.
- [21] Z. Liu, Q. Yu, Y. Zhao, R. He, M. Xu, S. Feng, S. Li, L. Zhou, L. Mai, *Chem. Soc. Rev.* **2019**, *48*, 285.
- [22] C. Huo, J. Wang, H. Fu, K.-Q. Peng, in *Photovoltaic Manufacturing: Etching, Texturing, and Cleaning*, (Ed.: M. F. Müller), Wiley-Scrivener, Beverly, MA, USA **2021**, pp. 1–41.
- [23] R. T. Pekarek, A. Affolter, L. L. Baranowski, J. Coyle, T. Hou, E. Sivonxay, B. A. Smith, R. D. McAuliffe, K. A. Persson, B. Key, C. Appleby, G. M. Veith, N. R. Neale, *J. Mater. Chem. A* **2020**, *8*, 7897.
- [24] N. E. Grant, A. I. Pointon, R. Jefferies, D. Hiller, Y. Han, R. Beanland, M. Walker, J. D. Murphy, *Nanoscale* **2020**, *12*, 17332.
- [25] D. E. Arreaga-Salas, A. K. Sra, K. Roodenko, Y. J. Chabal, C. L. Hinkle, *J. Phys. Chem. C* **2012**, *116*, 9072.
- [26] G. F. Cerofolini, A. Giussani, A. Modelli, D. Mascolo, D. Ruggiero, D. Narducci, E. Romano, *Appl. Surf. Sci.* **2008**, *254*, 5781.
- [27] Y. Chabal, *MRS Online Proc. Libr.* **1992**, *259*, 349.
- [28] M. T. McDowell, S. W. Lee, I. Ryu, H. Wu, W. D. Nix, J. W. Choi, Y. Cui, *Nano Lett.* **2011**, *11*, 4018.
- [29] R. Maddipati, C. Loka, K. S. Lee, *ACS Appl. Mater. Interfaces* **2020**, *12*, 54608.
- [30] S. Sim, P. Oh, S. Park, J. Cho, *Adv. Mater.* **2013**, *25*, 4498.
- [31] P. C. Soares, C. M. Lepienski, *J. Non-Cryst. Solids* **2004**, *348*, 139.
- [32] M. Schnabel, E. Arca, Y. Ha, C. Stetson, G. Teeter, S.-D. Han, P. Stradins, *ACS Appl. Energy Mater.* **2020**, *3*, 8842.
- [33] C. Cao, I. I. Abate, E. Sivonxay, B. Shyam, C. Jia, B. Moritz, T. P. Devereaux, K. A. Persson, H.-G. Steinrück, M. F. Toney, *Joule* **2019**, *3*, 762.

[1] A. Masias, J. Marcicki, W. A. Paxton, *ACS Energy Lett.* **2021**, *6*, 621.

- [34] K. W. Schroder, A. G. Dylla, S. J. Harris, L. J. Webb, K. J. Stevenson, *ACS Appl. Mater. Interfaces* **2014**, 6, 21510.
- [35] E. Ventosa, P. Wilde, A. H. Zinn, M. Trautmann, A. Ludwig, W. Schuhmann, *Chem. Commun.* **2016**, 52, 6825.
- [36] E. dos Santos Sardinha, M. R. Sternad, H. M. Wilkening, G. Wittstock, *ACS Appl. Energy Mater.* **2019**, 2, 1388.
- [37] C. L. Bentley, M. Kang, P. R. Unwin, *J. Am. Chem. Soc.* **2019**, 141, 2179.
- [38] C. L. Bentley, M. Kang, P. R. Unwin, *Curr. Opin. Electrochem.* **2017**, 6, 23.
- [39] O. J. Wahab, M. Kang, P. R. Unwin, *Curr. Opin. Electrochem.* **2020**, 22, 120.
- [40] N. Ebejer, A. G. Guell, S. C. S. Lai, K. McKelvey, M. E. Snowden, P. R. Unwin, *Annu. Rev. Anal. Chem.* **2013**, 6, 329.
- [41] A. Kumatani, Y. Takahashi, C. Miura, H. Ida, H. Inomata, H. Shiku, H. Munakata, K. Kanamura, T. Matsue, *Surf. Interface Anal.* **2018**, 51, 27.
- [42] Y. Takahashi, T. Yamashita, D. Takamatsu, A. Kumatani, T. Fukuma, *Chem. Commun.* **2020**, 56, 9324.
- [43] Y. Takahashi, Kumatani, H. Munakata, H. Inomata, K. Ito, K. Ino, H. Shiku, P. R. Unwin, Y. E. Korchev, K. Kanamura, T. Matsue, *Nat. Commun.* **2014**, 5, 5450.
- [44] B. Tao, I. J. McPherson, E. Daviddi, C. L. Bentley, P. R. Unwin, *ACS Sustainable Chem. Eng.* **2023**, 11, 1459.
- [45] B. Tao, L. C. Yule, E. Daviddi, C. L. Bentley, P. R. Unwin, *Angew. Chem., Int. Ed.* **2019**, 58, 4606.
- [46] E. B. Tetteh, D. Valavanis, E. Daviddi, X. Xu, C. Santana Santos, E. Ventosa, D. Martín-Yerga, W. Schuhmann, P. R. Unwin, *Angew. Chem., Int. Ed.* **2023**, 62, 202214493.
- [47] D. Martín-Yerga, M. Kang, P. R. Unwin, *ChemElectroChem* **2021**, 8, 4240.
- [48] D. Martín-Yerga, M. Bahri, M. E. Curd, X. Xu, W. Li, T. L. Burnett, P. J. Withers, B. L. Mehdi, N. D. Browning, P. R. Unwin, *Nat. Sci.* **2023**, 3, 20210607.
- [49] K. W. Schroder, H. Celio, L. J. Webb, K. J. Stevenson, *J. Phys. Chem. C* **2012**, 116, 19737.
- [50] M. Sternad, M. Forster, M. Wilkening, *Sci. Rep.* **2016**, 6, 31712.
- [51] Y. Horowitz, H. L. Han, P. N. Ross, G. A. Somorjai, *J. Am. Chem. Soc.* **2016**, 138, 726.
- [52] A. M. Haregewoin, T.-D. Shie, S. D. Lin, B.-J. Hwang, F.-M. Wang, *ECS Trans.* **2013**, 53, 23.
- [53] W. Xu, S. S. S. Vegunta, J. C. Flake, *J. Power Sources* **2011**, 196, 8583.
- [54] G. W. Trucks, K. Raghavachari, G. S. Higashi, Y. J. Chabal, *Phys. Rev. Lett.* **1990**, 65, 504.
- [55] V. Palermo, D. Jones, *Mater. Sci. Semicond. Process.* **2001**, 4, 437.
- [56] V. A. Burrows, Y. J. Chabal, G. S. Higashi, K. Raghavachari, S. B. Christman, *Appl. Phys. Lett.* **1988**, 53, 998.
- [57] Y. Chabal, G. Higashi, K. Raghavachari, V. Burrows, *J. Vac. Sci. Technol., A* **1989**, 7, 2104.
- [58] Y. J. Chabal, G. S. Higashi, K. Raghavachari, V. A. Burrows, *J. Vac. Sci. Technol., A* **1989**, 7, 2104.
- [59] A. Tokranov, R. Kumar, C. Li, S. Minne, X. Xiao, B. W. Sheldon, *Adv. Energy Mater.* **2016**, 6, 1502302.
- [60] A. Tokranov, B. W. Sheldon, C. Li, S. Minne, X. Xiao, *ACS Appl. Mater. Interfaces* **2014**, 6, 6672.
- [61] C. Stetson, M. Schnabel, Z. Li, S. P. Harvey, C.-S. Jiang, A. Norman, S. C. DeCaluwe, M. Al-Jassim, A. Burrell, *ACS Energy Lett.* **2020**, 5, 3657.
- [62] C. K. Chan, R. Ruffo, S. S. Hong, Y. Cui, *J. Power Sources* **2009**, 189, 1132.
- [63] A. Bordes, E. De Vito, C. Haon, A. Boulineau, A. Montani, P. Marcus, *Chem. Mater.* **2016**, 28, 1566.
- [64] J. Moon, B. Lee, M. Cho, K. Cho, *J. Power Sources* **2014**, 272, 1010.
- [65] E. Sivonxay, M. Aykol, K. A. Persson, *Electrochim. Acta* **2020**, 331, 135344.
- [66] G. Lener, M. Otero, D. E. Barraco, E. P. M. Leiva, *Electrochim. Acta* **2018**, 259, 1053.
- [67] G. Lener, A. A. Garcia-Blanco, O. Furlong, M. Nazzarro, K. Sapag, D. E. Barraco, E. P. M. Leiva, *Electrochim. Acta* **2018**, 279, 289.
- [68] Q. Sun, B. Zhang, Z.-W. Fu, *Appl. Surf. Sci.* **2008**, 254, 3774.
- [69] N. E. Grant, S. L. Pain, J. T. White, M. Walker, I. Prokes, J. D. Murphy, *ACS Appl. Energy Mater.* **2022**, 5, 1542.
- [70] C. L. Bentley, D. Perry, P. R. Unwin, *Anal. Chem.* **2018**, 90, 7700.